Nanoelectronics and Its New Materials – A NEW ERA OF NANOSCIENCE

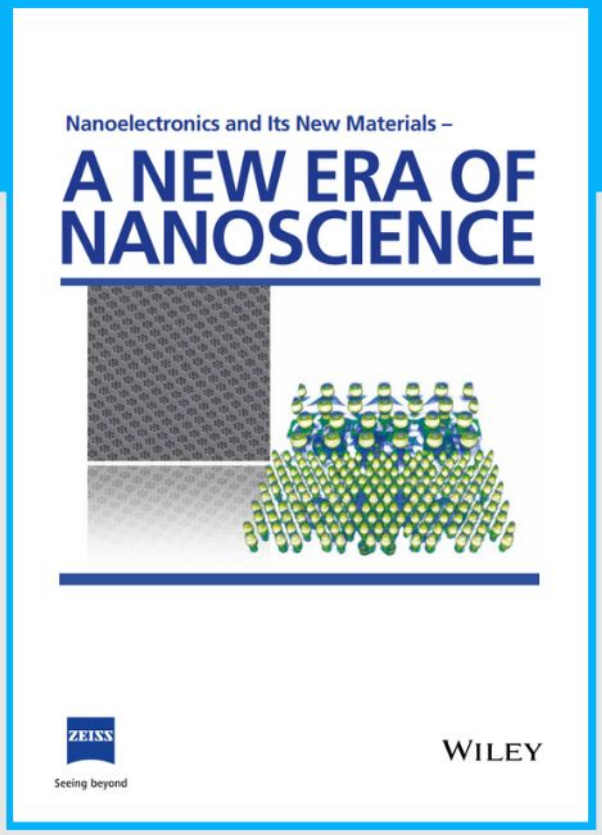

Discover the recent advances in electronics research and fundamental nanoscience.

Nanotechnology has become the driving force behind breakthroughs in engineering, materials science, physics, chemistry, and biological sciences. In this compendium, we delve into a wide range of novel applications that highlight recent advances in electronics research and fundamental nanoscience. From surface analysis and defect detection to tailored optical functionality and transparent nanowire electrodes, this eBook covers key topics that will revolutionize the future of electronics.

To get your hands on this valuable resource and unleash the power of nanotechnology, simply download the eBook now. Stay ahead of the curve and embrace the future of electronics with nanoscience as your guide.

ZEISS

Seeing beyond

WILEY

ADVANCED FUNCTIONAL MATERIALS
www.afm-journal.de

Mimosa-Inspired High-Sensitive and Multi-Responsive Starch Actuators

*Hao Hu, Mingzhe Nie, Massimiliano Galluzzi, Xuefeng Yu, and Xuemin Du**

Artificial intelligent actuators are extensively explored for emerging applications such as soft robots, human-machine interfaces, and biomedical devices. However, intelligent actuating systems based on synthesized polymers suffer from challenges in renewability, sustainability, and safety, while natural polymer-based actuators show limited capabilities and performances due to the presence of abundant hydrogen-bond lockers. Here this study reports a new hydrogen bond-mediated strategy to develop mimosa-inspired starch actuators (SA). By harnessing the unique features of gelatinization and abundant hydrogen bonds, these SA enable high-sensitivity and multi-responsive actuation in various scenarios. The non-gelatinized SA can be irreversibly programmed into diverse shapes, such as artificial flowers, bowl shapes, and helix structures, using near-infrared light. Furthermore, the gelatinized SA exhibit reversibly multi-responsive actuation when exposed to low humidity (10.2%), low temperature (37 °C), or low-energy light (0.42 W cm^{-2}). More importantly, the SA demonstrate robust applications in smart living, including artificial mimosa, intelligent lampshade, and morphing food. By overcoming the hydrogen-bond lockers inherent in natural polymers, SA open new avenues for next-generation recyclable materials and actuators, bringing them closer to practical applications.

1. Introduction

Artificial intelligent actuators that can change their shapes, colors, and/or generate motions in response to external stimuli are flourishing for their potential to revolutionize soft robots, human-machine interfaces, biomedical devices, and so on.[1–5] These intelligent actuating systems are usually fabricated with synthesized polymers such as stimuli-responsive hydrogels,[6–9] shape-memory polymers,[10–13] and liquid crystal elastomers,[14–16] by taking advantage of diverse mechanisms including anisotropic swelling, irreversible/reversible covalent bonds, and crystalline transitions. Such synthesized polymer components impart fascinating actuation including controllable shape morphing, multimode motions, and sensing the changing environment via naked-eye color shift upon exposure to various stimuli including light,[17–22] thermal,[23,24] humidity,[25–29] chemicals,[30–32] electric, and magnetic fields.[33–35] However, these polymer-based actuators suffer from challenges in renewability, sustainability, and safety, especially applied in robotic, biomedical, food, and home furnishing domains.[2,3,36]

In nature, various biological systems can dynamically change their shapes, colors, and motions to adapt to a complex environment. For example, mimosa can rapidly close their leaves in response to dangerous stimuli including sunlight, humidity, or touch.[9,37,38] These intelligent actuation behaviors are strongly related to their responsive tissues formed by natural materials, which can absorb/dehydrate water upon exposure to these stimuli. Hence, one of the ultimate goals of artificial intelligent actuators is to use natural materials to achieve living organism-like multi-responsive actuating capability.[2,9,39] To mimic the natural biological system behaviors, several natural polymers have been developed into various actuators, however, their actuation behaviors are limited to mono-responsive capability and simple performances.[40–42] As one of the most promising natural materials, starch has been widely used in food, biomedical, and industrial fields not only because of its affordability, renewability, biocompatibility, and biodegradability, but also owing to its unique gelatinization feature (i.e., heat-induced disintegration of starch granules in water) resulted from the abundant intermolecular and intramolecular hydrogen bonds.[43–49] Paradoxically, these abundant and strong hydrogen bonds endow starch with the above distinctive properties impossible in both synthesized and other natural polymers, however, the inherent flexibility in imparting actuation behaviors through mediating hydrogen bonds is thus compromised.[50] Current strategies for mediating the inherent hydrogen bonds in starch rely on chemical modifications or introducing synthesized polymers, both of which would inevitably cause deterioration in recyclability, biocompatibility, and biodegradability, thus making them

H. Hu, M. Nie, X. Du
Institute of Biomedical & Health Engineering
Shenzhen Institute of Advanced Technology (SIAT)
Chinese Academy of Sciences (CAS)
Shenzhen 518055, P. R. China
E-mail: xm.du@siat.ac.cn

M. Galluzzi, X. Yu
Institute of Advanced Materials Science and Engineering
Shenzhen Institute of Advanced Technology (SIAT)
Chinese Academy of Sciences (CAS)
Shenzhen P. R. China

The ORCID identification number(s) for the author(s) of this article can be found under https://doi.org/10.1002/adfm.202304634

DOI: 10.1002/adfm.202304634

challenging for practical applications.[51,52] Despite the above significant progress, developing multi-responsive starch actuators via mediating its intrinsic hydrogen bonds remains a major challenge and unexplored.

Here, we report an innovative hydrogen bond-mediated strategy for developing mimosa-inspired multi-responsive starch actuators (SA), which consist of three components (**Figure 1**A, B): 1) starch owing to its unique heat-induced gelatinization feature (Figures S1 and S2, Supporting Information); 2) sodium alginate for its natural source and similar molecule structures; 3) microsized liquid metal particles (LMPs) owing to its excellent photothermal behaviors.[53,54] Such rational design imparts unprecedented irreversible-to-reversible actuating capability for one SA system (Figure 1C–F). We demonstrate that the non-gelatinized SA can be irreversibly programmed into diverse Gaussian curvatures (e.g., artificial flower, bowl shape, short-side rolling, long-side rolling, and helix structures) by 808-nm near-infrared (NIR) light owing to the photothermal-induced unlocking of hydrogen bonds (partial gelatinization of SA). Furthermore, we also show that the gelatinized SA exhibit reversibly multi-responsive actuating capability owing to the reversibility of the locking/unlocking hydrogen bonds upon exposure to ultralow relative humidity (≈10.2%), near human body temperature (≈37 °C), or low-energy NIR irradiation (0.42 W cm^{-2}), and it can last for 1000 cycles without noticeable fatigue. More importantly, we further extend the SA to smart living, ranging from artificial mimosa to intelligent lampshade with superior environmental sensing functions, to 2D-to-3D morphing food. The SA overcome the hydrogen-bond lockers inherent in natural polymers and would open new avenues for the next-generation recyclable materials and actuators, bringing them one step close to practical applications.

2. Results

2.1. Fabrication of SA

We adopted a facile casting method to prepare two typical SA (i.e., non-gelatinized SA, and gelatinized SA, see Methods). To fabricate the non-gelatinized SA, we first prepared a well-dispersed composite precursor of raw starch granules, sodium alginate, and pre-synthesized LMPs, followed by filling the precursor into a home-made device, and then a complete solidification (Figure S3A, Supporting Information). After immersing into 0.1 M calcium chloride solution for 2 min, the Ca^{2+}-crosslinked composite film can be easily and completely peeled off from the device, which shows excellent integrity compared to the format without adding sodium alginate as shown by optical images (Figure S3B, Supporting Information). Scanning electron microscopy (SEM) image evidenced the uniform dispersion of starch granules within the loose network of physically crosslinked sodium alginate, which is ascribed to the high miscibility of starch with sodium alginate (Figure 1C, Figure S3C, Supporting Information). In addition, energy-dispersive X-ray spectroscopy (EDS) images show a well dispersion of LMPs within the composite film owing to the strong interactions between the LMPs and abundant hydroxyl groups (OH) in the polymer chains.[55]

Different from the preparation process of the former non-gelatinized SA, the gelatinized SA were prepared by casting the well-dispersed precursor of pre-gelatinized starch, sodium alginate, and LMPs into the homemade device (Figure S4A, Supporting Information). After drying for 12 h at room temperature, the composite film was facilely peeled off from the device, which exhibits high flexibility and uniformity as shown by optical, SEM, and EDS images (Figure 1E, Figure S4B,C, Supporting Information). Notably, the cross-section morphology of the composite film indicates that the gelatinized starch and sodium alginate form a tightly interconnected network, which is attributed to the existence of massive hydrogen-bond interactions from the gelatinized starch chains and sodium alginate chains. Such non-gelatinized and gelatinized status of starch in the composite films would impart two unprecedented actuation behaviors in one system.

2.2. Programmed Shape Morphing of the Non-Gelatinized SA

We then evaluated the photothermal-induced programmable shape morphing of the non-gelatinized SA. Upon exposure to NIR light, the embedded LMPs rapidly absorb NIR light and convert it into spatial temperature rise above the gelatinization temperature, which results in the gelatinization of the raw starch granules at the irradiated area (**Figure 2**A, Figure S5, Supporting Information).[43] Such photothermal-induced partial gelatinization of starch can be evidenced by SEM images. As shown in Figure 2B, the starch granules remain integrated structures before NIR irradiation, while the granules are disintegrated into porous structures after NIR irradiation. Notably, the NIR irradiation induces a gelatinization gradient across the thickness of the SA film, in which the top surface shows porous structures, whereas the bottom surface exhibits integrate starch granules. This photothermal-induced gelatinization gradient of starch can be further verified by Young's modulus mapping (Figure 2C). Before NIR irradiation, Young's modulus for the top surface (19.44 ± 2.23 MPa) is slightly higher than that of the bottom surface (6.45 ± 1.11 MPa) owing to the crosslinking gradient across the film thickness (Figure S6, Supporting Information).[40,41] After NIR irradiation, Young's modulus for the top surface sharply decreases (0.96 ± 0.25 MPa), whereas Young's modulus for the bottom surface remains unchanged (6.76 ± 1.60 MPa). Such photothermal-induced gelatinization gradient leads to swelling difference across the thickness of SA film that introduces out-of-plane stress and herein bending against the light direction, and the bending angle can be tuned by the film thickness, irradiation time, LMPs concentration/distribution, or the irradiation area (Figures S7–S9, Supporting Information).

We next revealed the mechanism of the photothermal-induced gelatinization of starch at the molecular level. As schemed in Figure 2D, the NIR irradiation causes the disintegration of the crystalline phase into an amorphous phase in the raw starch granules, which is ascribed to the photothermal-induced irreversible breakdown of the intermolecular and intramolecular hydrogen bonds in the starch chains, thus releasing large amount -OH groups. These unlocked -OH groups form new hydrogen bonds with water molecules in the environment, thus leading to

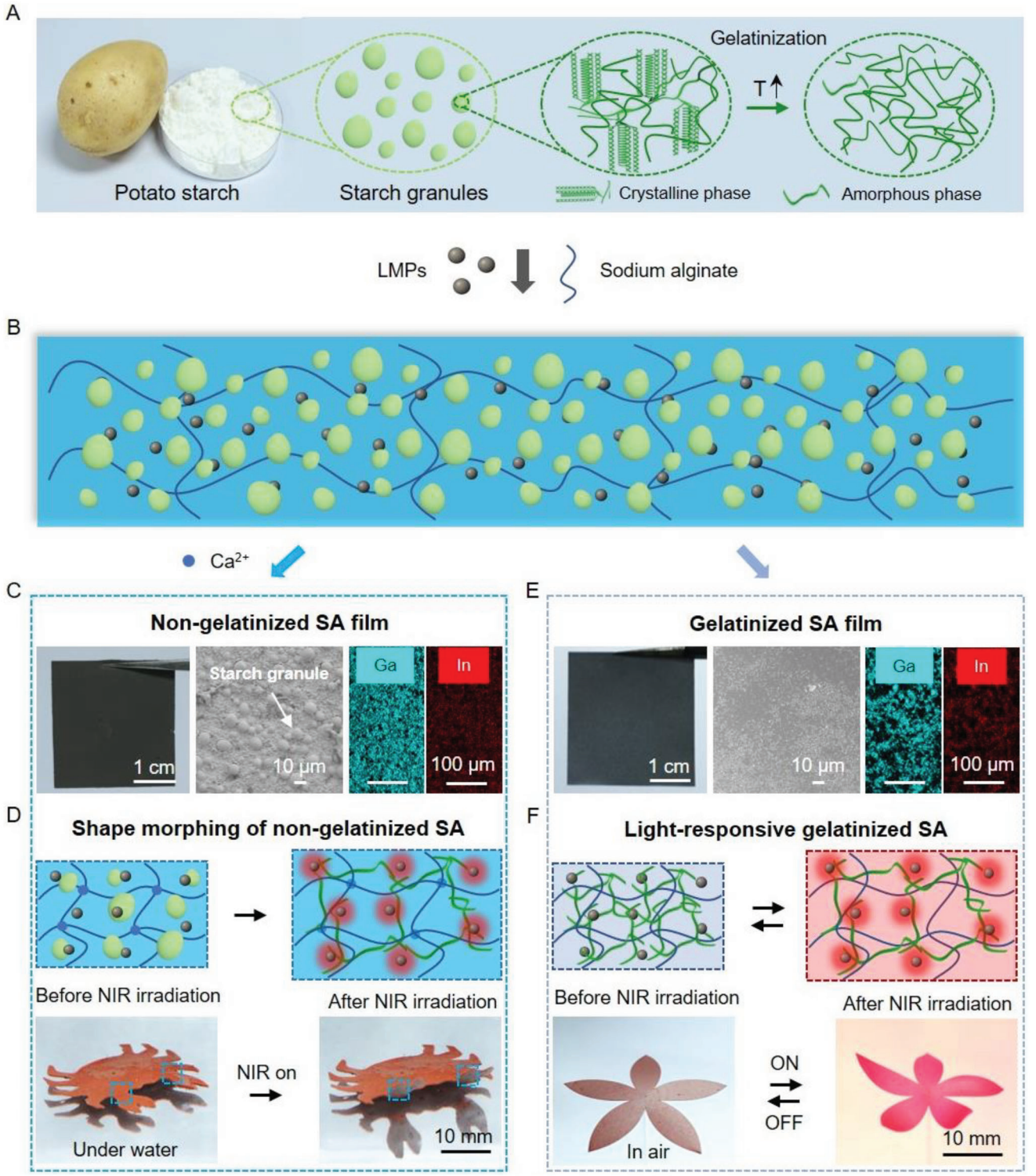

Figure 1. Fabrication and principle of the SA system. A) Photograph of potato starch and schematic illustration of starch granule structure together with its structure transitions during thermal-induced gelatinization. B) Schematic diagram of the SA compositions. C) Photograph of the non-gelatinized SA film, SEM image of the surface morphology, and EDS mapping of the embedded Ga-In LMPs in the film. D) Schematic illustration of light-induced irreversibly partial gelatinization of the non-gelatinized SA, and photograph of a crab with light-induced waving claw in water (430-μm thickness, 4.8 W cm^{-2}). E) Photograph of the gelatinized SA film, SEM image of the surface morphology, and EDS mapping of the embedded Ga-In LMPs in the film. F) Schematic illustration of light-responsive gelatinized SA, and photograph of an artificial flower with reversibly light-responsive actuation in air (26-μm thickness, 0.24 W cm^{-2}).

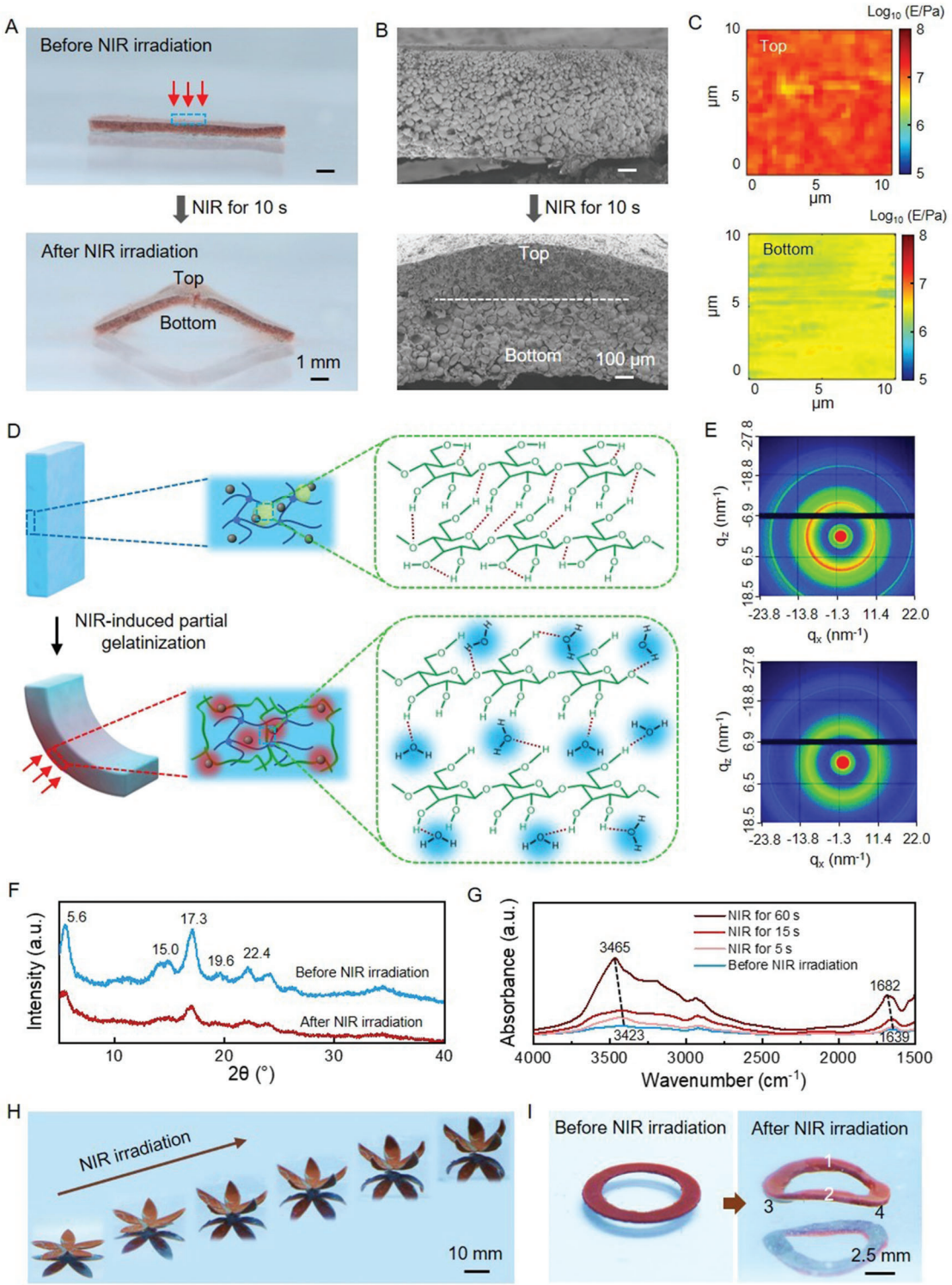

Figure 2. Programmed shape-morphing mechanism and behaviors. A) Photograph of light-induced shape morphing of the non-gelatinized SA film underwater. B) SEM images of the cross-section morphology of the non-gelatinized SA film (430-μm thickness) before and after NIR irradiation (4.8 W cm^{-2}) for 10 s. C) Young's modulus mapping (top and bottom surface) for the non-gelatinized SA film after NIR irradiation (4.8 W cm^{-2}) for 10 s. D) Schematic illustration of the shape-morphing mechanism. E) 2D-WAXD patterns of the non-gelatinized SA film before and after NIR irradiation. F) 1D-WAXD profiles of the non-gelatinized SA film before and after NIR irradiation. G) NIR irradiation-dependent FTIR spectra for the non-gelatinized SA film (irradiation time from 0 to 60 s). H) Light-induced programmable folding of an artificial flower via illuminating below every petal (4.8 W cm^{-2}, 430-μm thickness). I) Light-induced controllable shape morphing of a planar ring (4.8 W cm^{-2}, 430-μm thickness) via illuminating above (sites 1 and 2) and below (sites 3 and 4), respectively.

local swelling at the irradiated area and herein bending of the SA film owing to the gelatinization gradient across the thickness. Such NIR irradiation-induced structure transitions of the raw starch granules can be evidenced by 2D wide-angle X-ray diffraction (2D-WAXD) analysis. As shown in Figure 2E, the 2D-WAXD patterns show obvious inner-to-outer diffraction rings before NIR irradiation, indicating the crystalline phase in the raw starch granules. After NIR irradiation, the diffraction rings become weaker, and some diffraction rings even diminish, suggesting the disintegration of the crystalline phase in the starch granules. The variations of characteristic diffraction peaks can be further evidenced by the 1D-WAXD intensity profiles. Figure 2F shows that the characteristic diffraction peaks are observed at 2θ of 5.6, 15.0, 17.3, 19.6, and 22.4° in the non-gelatinized SA before NIR irradiation, respectively. After NIR irradiation, these characteristic diffraction peaks decrease or even disappear, suggesting transitions of the crystalline phase into the amorphous phase.[56] These photothermal-induced phase transitions are ascribed to the irreversible breakdown of the intermolecular and intramolecular hydrogen bonds, which can be clarified by attenuated total reflectance-Fourier transform infrared (ATR-FTIR) spectra. Figure 2G shows that the -OH bending vibration absorption peak at 1639 cm^{-1} and stretching vibration absorption peak at 3423 cm^{-1} increase and redshift with increasing the NIR irradiation time. These results can be ascribed to the increase of liberation of -OH groups on the starch chains and the formation of new hydrogen-bond networks with water molecules.[57] Such results suggest the intrinsic hydrogen bonds in starch and its irreversible gelatinization can be facilely mediated by NIR irradiation.

Based on the above unique feature of starch, we can achieve controllable and complex shape morphing. As shown in Figure S10, Supporting Information, a planar round film can transform into a bowl structure via irradiation at the center of the film. By increasing the irradiation area or introducing irradiation patterns, planar SA films can be easily programmed into various Gaussian curvatures by a laser beam. As shown in Figure S11, Supporting Information, specific gelatinized patterns (i.e., well-aligned line arrays at angles of 0°, 45°, and 90°) can be facilely written into the non-gelatinized SA, thus imparting diverse and controllable shape morphing, including short-side rolling, long-side rolling, and helix structures. Furthermore, artificial flowers, fingers, limbs, and box exhibit precisely programmable shape morphing upon exposure to a step-by-step NIR irradiation in the same direction (Figure 2H, Figure S12, Supporting Information). It is worth noting that a planar ring film can be programmed into a complex curvature by a step-by-step NIR irradiation at both the top and bottom directions (Figure 2I). Such photothermal-induced partial gelatinization of starch increases local swelling behaviors, and allows us to edit the starch morphing by light facilely.

2.3. Multi-Responsive Actuation of the Gelatinized SA

Aside from the irreversible shape morphing of the non-gelatinized SA, we further investigate the multi-responsive actuation of the completely gelatinized SA. When a gelatinized film was placed on a low-moist filter paper, the film rapidly bends against the moist source in seconds owing to the non-uniform water absorption and thus different swelling between the exposed and non-exposed sides (**Figure 3**A, Supporting Information). When moved away from the moist source, the film fast recovers to its initial planar shape (Movie S1, Supporting Information). Notably, the gelatinized SA film can sense a relative humidity as low as 10.2%. In addition, the gelatinized film demonstrates similar actuation behaviors when placed on a hot platform or exposed to NIR irradiation. As shown in Figure 3B,C, the gelatinized film fast bends against the heat source or NIR light in seconds owing to the thermal gradient-induced expansion difference between the exposed and non-exposed sides (Figures S13 and S14, Supporting Information). Remarkably, the rapid actuation can be induced at near human body temperature (37 °C) or by exposure to a very low laser power density (0.42 W cm^{-2}). Such actuation behaviors can be adjusted by varying the film thickness, relative humidity, exposure thermal, and LMPs concentration (Figures S15 and S16, Supporting Information).

Notably, these superior multi-responsive actuation behaviors of the gelatinized SA are attributed to the fast unlocking and locking of hydrogen bonds in the polymer network. As schemed in Figure 3D, the gelatinized SA film shows tight polymer networks owing to the abundant intermolecular hydrogen bonds before exposure to a specific stimulus. After exposure to moisture, water molecules fast diffuse into the exposed side of the film, unlock the intermolecular hydrogen bonds, and form new hydrogen bonds with the -OH groups in the starch and sodium alginate chains, while the non-exposed side remains with tight polymer networks owing to slow water absorption. Such different water absorption leads to anisotropic swelling and thus bending of the SA film.[25,29] This process can be evidenced by ATR-FTIR spectra when exposed to moisture for a different time. Figure 3E shows that the -OH bending vibration absorption peak at 1602 cm^{-1} and stretching vibration absorption peak at 3268 cm^{-1} increase and evolution with increasing the vapor exposure time, which can be attributed to the increase of bonded water.[57] Similarly, the intermolecular hydrogen bonds in the SA film can also be mediated by thermal or photothermal exposure, which increases the thermal movements of polymer chains in the exposed side. However, the non-exposed side remains tight polymer networks. Such different polymer networks lead to anisotropic expansion and thus bending of the SA film. Figure 3F shows that the -OH bending vibration absorption peak at 1629 cm^{-1} and stretching vibration absorption peak at 3510 cm^{-1} decrease and blue shift with increasing the heating temperature, which can be ascribed to the unlocking of the intermolecular hydrogen bonds.[58] Such fast and reversible locking and unlocking of hydrogen bonds endow the high-sensitive and reversible actuation behaviors. As shown in Figure 3G, a butterfly-like gelatinized film first shows a planar structure, then bends as moving near a fingertip, and finally flaps its wings continuously on the fingertip owing to its high sensitivity to the low moisture and thermal of the fingertip (Movie S2, Supporting Information). Notably, the actuation can last for more than 1000 cycles without apparent fatigue (Figure 3H). Such living organism-like mechanical properties and high-sensitive, multi-responsive actuating capabilities of SA would open new avenues for various practical applications (Figure S17, Supporting Information).

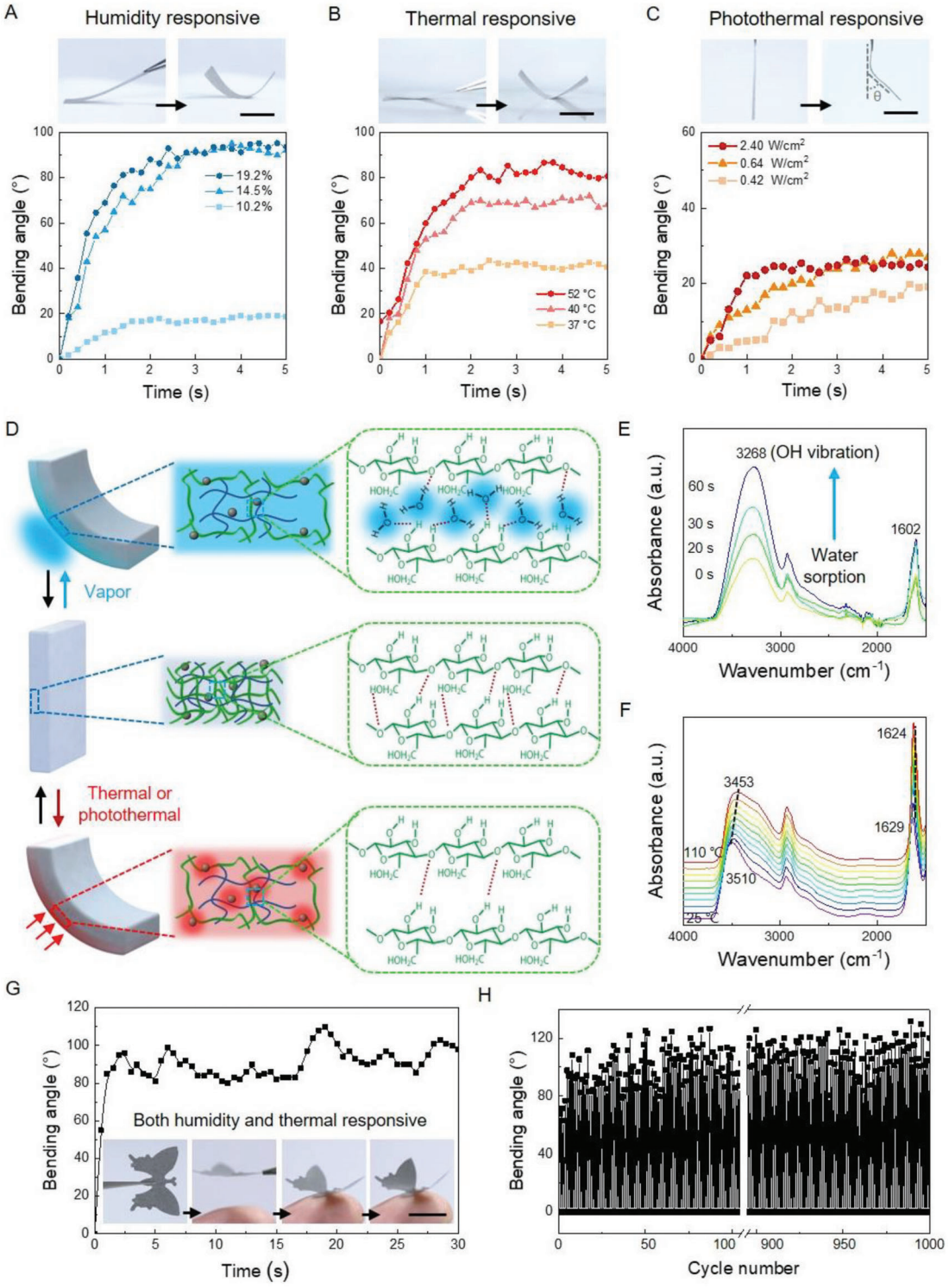

Figure 3. Mechanism and behaviors of multi-responsive actuation. A) Humidity-induced shape morphing of the gelatinized SA film as exposure to various relative humidity from 10.2% to 19.2%. The actuation speed is as large as 66.5° s^{-1} for a relative humidity of 14.5%. B) Thermal-induced shape morphing of the gelatinized SA film as exposure to various temperatures from 37 to 52 °C. The actuation speed is as large as 56.5° s^{-1} for the relative humidity of 40 °C. C) Photothermal-induced shape morphing of the gelatinized SA film as exposure to various laser power densities from 0.42 to 2.4 W cm^{-2}. The actuation speed is as large as 22.3° s^{-1} for the relative humidity of 0.64 W cm^{-2}. D) Schematic illustration of the multi-responsive actuation mechanism. E) Moisture-dependent ATR-FTIR spectra for the gelatinized SA film as exposure to water vapor from 0 to 60 s. F) Temperature-dependent FTIR spectra for the gelatinized SA film as exposure to temperatures from 25 to 110 °C. G) The images of an artificial butterfly flapping on a fingertip, and the corresponding changes of bending angle. H) The durability of long-term actuation of the gelatinized SA film after 1000 cycles of 35-°C water vapor stimulation. Scale bars: 10 mm.

2.4. Smart Living Applications

Leveraging on the former multi-responsive properties, the SA can be used for smart homes and morphing food. First, the gelatinized SA can serve as an artificial mimosa, which can interact with the changing environment. As shown in **Figure 4**A, natural mimosa leaves first open, and then close once touched by a fingertip, of which open-to-close progress needs 15 s (Movie S3, Supporting Information). Superior to the natural mimosa, our artificial mimosa demonstrates high sensitivity to stimuli, and it takes only 4 s to close its leaves as exposed to a fingertip (Figure 4A, Movie S4, Supporting Information). Furthermore, after deposition with an electrode array on the leaves, our artificial mimosa not only can sense the changing environment, but also provide simultaneous feedback via capacity variations, which can monitor the environment changes to meet the strict requirements of specific scenarios, such as space labs and polar regions (Figure 4B, Figure S18, Supporting Information). Second, the gelatinized SA can also be used for a smart lampshade (Figure 4C,D). As shown in Figure 4D, the gelatinized SA-based lampshade first closes, and then opens by switching on the light. Switching off the light, the lampshade then closes correspondingly (Movie S5, Supporting Information). This on-off light-induced open-to-close lampshade is attributed to the photothermal-induced rapid actuation of the gelatinized SA as shown in Figure 4E. Such distinctive features enable light-induced rolling and creeping of gelatinized SA (Figure S19, Movies S6 and S7, Supporting Information). Third, a food-grade artificial octopus can be configured from planar structures into 3D structures upon exposure to NIR irradiation. As shown in Figure 4F and Movie S8, Supporting Information, food-grade cuttlefish powder embedded in the flour-based octopus can also convert NIR light into local heat, resulting in local gelatinization and herein expansion of the octopus. Upon continuous NIR irradiation, the whole body of the octopus expands and reconfigures correspondingly, which opens new and facile avenues for smart food.[59] Notably, such SA composed with natural source elements demonstrates superior biodegradability (Figure 4G), enabling an innovative sustainable strategy for the development of next-generation intelligent actuators.[60]

3. Discussion

In summary, we developed a new strategy for preparing multi-responsive and biodegradable starch actuators that harness their unique features of both gelatinization and intrinsic hydrogen bonds, which overcomes the bottlenecks inherent in conventional polymer-based actuators owing to the robust capability of real-time hydrogen bond mediation via light, humidity, and temperature. We show that the SA demonstrate precise programmable morphing behaviors, and superior actuating capabilities, including highly sensitive to ultralow humidity (≈10.2%), human-body temperature (≈37 °C), and low-energy NIR irradiation (0.42 W cm^{-2}) but fast and non-fatigue actuation behaviors (1000 cycles). The highly sensitive, multi-responsive, and irreversible-to-reversible actuation imparts their distinctive applications in environmental monitoring, smart lampshade, and smart food. The natural source, facile preparation, and unique features of the SA would open new avenues for environment-friendly actuating materials and smart life.

4. Experimental Section

Materials: Potato starch (M_W: 342.30 g mol^{-1}) and sodium alginate were purchased from Sigma-Aldrich (Missouri, USA). Methylcellulose (MC) was purchased from Alfa Aesar Chemical Reagent Co. Ltd. (Tianjin, China). Liquid metal (LM) eutectic gallium-indium (75.5 wt% Ga and 24.5 wt% In) was purchased from Fanyada Electronic Technology Co. Ltd. (Zhenjiang, China). Calcium chloride ($CaCl_2$) was purchased from Sinopharm Chemical Reagent Co. Ltd. (Shanghai, China). Congo red was purchased from Shanghai Macklin Biochemical Co. Ltd. (Shanghai, China). Ultrapure water provided by a Purelab flex water purification system (≈18.2 MΩ cm, High Wycombe, UK) was used in the experiments.

Preparation of Liquid Metal Particles: The LMPs were synthesized according to previous work.[53,54,61] Briefly, 0.1 wt% MC solution was prepared by dissolving 0.1 g MC in 99.9 g hot water (90 °C) for 30 min, and then cooled to room temperature (25 °C). Afterward, 1.0 g LM was added into 9.0 g MC solution (0.1 wt%), and the mixture was then sonicated in an ice bath for 5 h. The obtained LMPs solution (10.0 wt%) was used in the following experiments.

Preparation of Non-Gelatinized Starch Actuator Film: First, a non-gelatinized SA precursor was prepared by uniformly mixing 30.0 mL aqueous suspension of starch granules (20.0 wt%), 10.0 mL sodium alginate aqueous solution (2.0 wt%), and 6.0 mL of LMPs solution (10.0 wt%). Second, 3.0 mL non-gelatinized SA precursor was poured into a homemade device (40.0 mm × 40.0 mm × 2.0 mm),[8,40,41] followed by evaporation at a fume hood at room temperature for 5 h. Third, the non-gelatinized SA film was crosslinked in a 0.1 M $CaCl_2$ solution for 2 min. Finally, the non-gelatinized SA film with a thickness of 430 µm was peeled off from the device, and then immersed in water for the following experiments. Notably, the non-gelatinized SA films with various thicknesses (138, 280, 544, and 682 µm) and various LMPs concentrations (5, 10, and 15 wt%) were prepared in the same manner as mentioned above. Unless otherwise specified, the non-gelatinized SA film with a thickness of 430 µm was used for the following experiments. For better visualization, dyed non-gelatinized SA films with Congo red were prepared.

Preparation of Gelatinized Starch Actuator Film: First, 2.0 wt% gelatinized starch solution was prepared by heating the aqueous suspension of starch granules at 80 °C for 30 min under constant stirring. Second, a gelatinized SA precursor was prepared by uniformly mixing 37.8 mL gelatinized starch solution (2.0 wt%), 18.1 mL sodium alginate aqueous solution (2.0 wt%), and 1.0 mL LMPs solution (10.0 wt%). Third, 3.0 mL gelatinized SA precursor was poured into the homemade device (40.0 mm × 40.0 mm × 2.0 mm), followed by evaporation at a fume hood at room temperature for 12 h. Finally, the gelatinized SA film with a thickness of 26 µm was peeled off from the device, and then sealed and stored for the following experiments. Notably, the gelatinized SA films with various thicknesses (35, 48, 58, and 72 µm) and various LMPs concentrations (5, 10, and 15 wt%) were prepared in the same manner as mentioned above. Unless otherwise specified, the non-gelatinized SA film with a thickness of 26 µm was used for the following experiments.

Programmable Shape Morphing of Non-Gelatinized Starch Actuator Film: To study the relationship between the shape morphing and the thickness of the non-gelatinized SA film, the non-gelatinized SA films with various thicknesses (138, 280, 430, 544, and 682 µm) were first cut into sheets (3.0 mm × 10.0 mm), which were then partially gelatinized via exposing to near-infrared (NIR) irradiation (808 nm, 4.8 W cm^{-2}) for 10 s, respectively. Afterward, the bending angles were measured after immersing the partially gelatinized SA films in water for 30 min.

To study the relationship between the shape morphing and the NIR irradiation time, the non-gelatinized SA films were cut into sheets (10.0 mm × 30.0 mm × 430 µm), which were then partially gelatinized via exposure to near-infrared (NIR) irradiation (808 nm, 4.8 W cm^{-2}) for 0, 5, 10, 15, and 20 s, respectively. Then, the bending angles were measured after immersing the partially gelatinized SA films in water for 30 min.

To study the relationship between the shape morphing and the NIR irradiation area, the non-gelatinized SA films were cut into sheets (3.0 mm × 10.0 mm × 430 µm), which were then partially gelatinized via exposure to near-infrared (NIR) irradiation (808 nm, 4.8 W cm^{-2}) with various

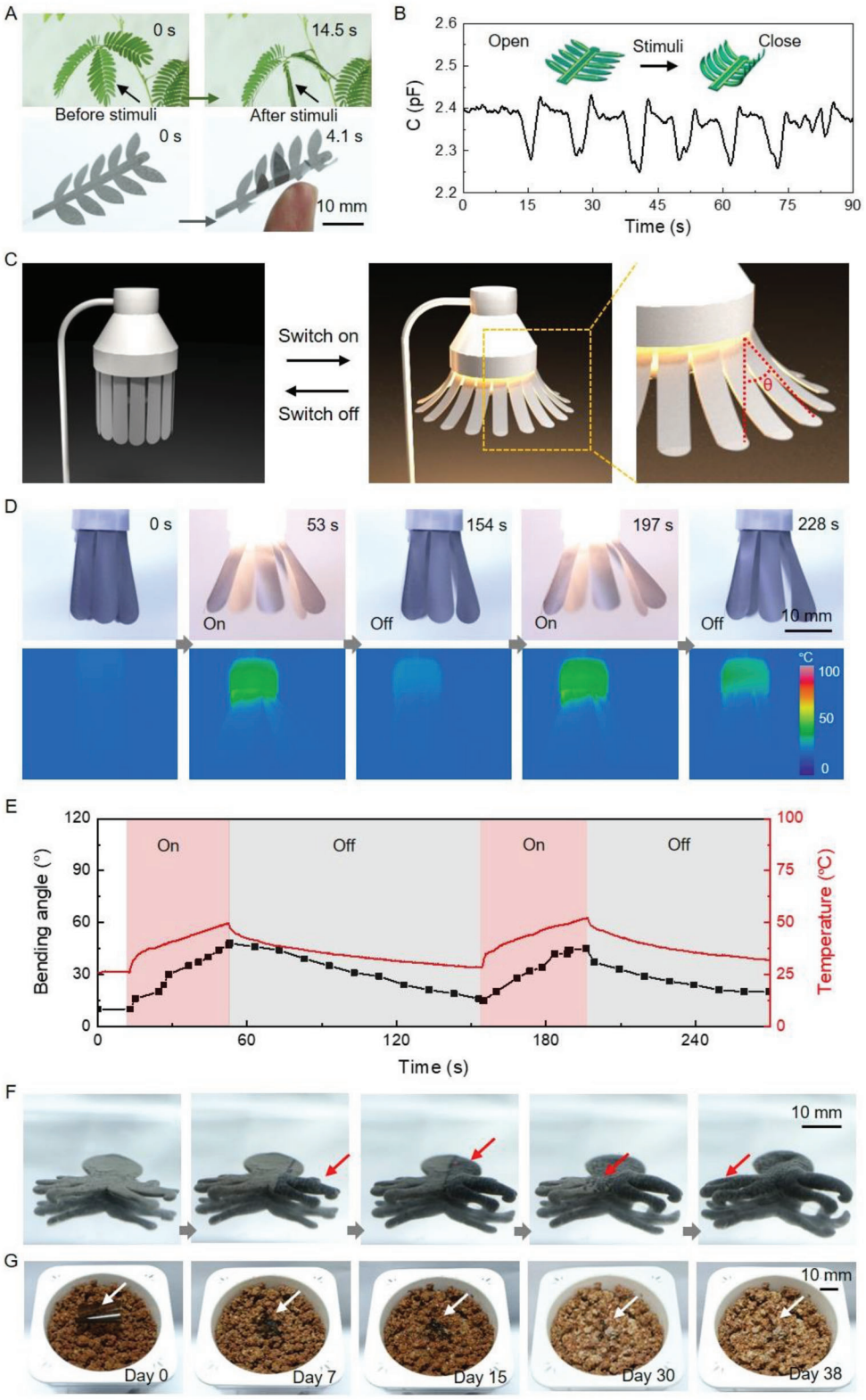

Figure 4. Multi-responsive SA for smart homes and morphing food. A) Fingertip-induced actuation of both mimosa and artificial mimosa. B) An artificial mimosa not only can change shape but also can sense touch stimuli after being designed with electrode arrays on the leaves. C) Schematic illustration of the smart lampshade. D) Photographs and infrared thermal images of the actuation of the lampshade via on-off light. E) The bending angle and temperature change as on-off light. F) Light-induced dynamic shape configuration of an artificial octopus under water upon exposure to 48 W cm^{-2} NIR irradiation. G) Biodegradability photographs of the non-gelatinized SA film in soil, indicating its degradation within 38 days.

irradiated areas of 0, 16.8, 22.5, 36.9, 66.3, 90.9, and 127.8 mm^2, respectively. Then, the bending angles were measured after immersing the partially gelatinized SA films in water for 30 min.

To demonstrate the programmable shape morphing, the non-gelatinized SA films were cut into crab, flower, hand, human, round, and ring shapes, which were then irradiated by NIR laser (808 nm, 4.8 W cm^{-2}) at specific sites. To further demonstrate their potential applications in smart food, 100 g flour, 2 g cuttlefish powders, 60 mL water, and 5 mL edible oil were mixed, and then kneaded into a dough sheet. Afterward, the dough sheet was cast into an octopus-shaped mold, and then peeled off from the mold with an octopus shape (2 mm thickness). The 2D artificial octopus under water could transform into a 3D configuration upon exposure to a continuous and complete NIR irradiation (48 W cm^{-2}).

Multi-Responsive Actuation of Gelatinized SA: To reveal the relationship between the bending angle and the moisture content, the relative humidity (H) of the filter paper surface can be simply determined by the following equation:

$$H = H_1 - H_0 \quad (1)$$

where H_0 and H_1 are the relative humilities of the filter paper before and after spraying with water. The relative humidity of the filter paper surface was recorded by a digital humidity meter (UT333S). To study the humidity-responsive actuation, the gelatinized SA stripes (5.0 mm × 20.0 mm × 26 µm) were put onto filter papers, which were sprayed with different moisture content (relative humidity of the surface: 10.2%, 14.5%, 19.2%, 29.2%, 35.4%, and 45.2%). Then, the maximum bending angles were recorded by a digital camera (Canon EOS 7D Mark II, Japan) at room temperature. In addition, the maximum bending angles of the gelatinized SA stripes (5.0 mm × 20.0 mm) with various thicknesses (35, 48, 58, and 72 µm) were also recorded in the same manner as mentioned above when exposed to a relative humidity of 19.2%.

To study the thermal-responsive actuation, the gelatinized SA films (5.0 mm × 20.0 mm × 26 µm) were placed on the surface of a magnetic stirrer with different temperatures (37, 40, 52, 60, and 70 °C). Then, the maximum bending angles were recorded by a digital camera (Canon EOS 7D Mark II, Japan). In addition, the maximum bending angles of the gelatinized SA stripes (5.0 mm × 20.0 mm) with various thicknesses (35, 48, 58, and 72 µm) were also recorded in the same manner as mentioned above when exposed to a specific temperature of 50 °C.

To study the photothermal-responsive actuation, the gelatinized SA stripes (5.0 mm × 20.0 mm × 26 µm) were irradiated by a NIR laser with different power densities (0.42, 0.64, and 2.4 W cm^{-2}). Then, the maximum bending angles were recorded by a digital camera (Canon EOS 7D Mark II, Japan).

To demonstrate the multi-responsive actuation, the gelatinized SA films were cut into flower, butterfly, and mimosa leaves shapes, which were then exposed to certain stimuli. The actuation cycles of a gelatinized SA stripe (5.0 mm × 20.0 mm × 26 µm) were recorded by a digital camera (Canon EOS 7D Mark II, Japan) upon exposure to 35 °C water vapor via a homemade setup according to our previous work.[30,32] In addition, gold electrode arrays onto the leaves of an artificial mimosa were further prepared with a sputter coater (20 mA, 240 s; Q150R ES coater, Quorum, UK) and a homemade mask. The capacity change of the artificial mimosa upon exposure to certain stimuli was recorded by an LCR meter (50 Hz-100 KHz, Changzhou Tonghui Electronic Co. Ltd.) equipped with a test fixture (TH26011CS, Changzhou Tonghui Electronic Co. Ltd.). For studying their potential applications in smart homes, the gelatinized SA film was cut into a lampshade and then adhered around a lamp (0.75 W), which was connected to a facile circuit. Then, the bending angle alterations were recorded by a digital camera (Canon EOS 7D Mark II, Japan) as on-off switching of light.

Biodegradability of the Non-Gelatinized SA Film: The decomposition degree of the non-gelatinized SA film was facilely observed through visual inspection. First, a gelatinized SA precursor was prepared by uniformly mixing 37.8-mL gelatinized starch solution (2.0 wt%), 18.1-mL SA solution (2.0 wt%), and 1.0-mL cuttlefish solution (10.0 wt%). Second, 3.0-mL gelatinized SA precursor was poured into a homemade device (40.0 mm × 40.0 mm × 2.0 mm), followed by evaporation at a fume hood for 18 h. Third, a gelatinized SA film (30.0 mm × 30.0 mm × 26.0 µm) was placed in a basin filled with moist soil. The decomposition process was recorded by a digital camera (Canon EOS 7D Mark II, Japan).

Characterizations: The thicknesses of SA films were measured by an optical microscope (Nikon Ni-U, Japan). The morphologies of the cross-sectional composited hydrogel films were characterized by a field-emission-scanning electron microscope (FE-SEM, Sigma, Carl Zeiss 300, Germany). The photographs of the SA films were recorded by a digital camera (Canon, EOS 7D Mark II, Japan). An 808-nm near-infrared (NIR) laser (FU808AD1000-GD22, SZ laser, 1000 mW, Shenzhen Zhonglai Technology Co. Ltd.) was used in the experiments. The NIR laser power density was determined by a Thorlabs PM100D optical power meter equipped with a Thorlabs S425C photodiode sensor (diameter, 25.4 mm; power range, 2 mW to 10 W; wavelength range, 190 nm to 20 µm). The infrared imaging photographs and the temperature alterations were recorded by an infrared thermometer (R550Pro, 21 µm, NEC, Japan). The local elasticities of SA films were probed with a commercial atomic force microscope CypherES (AFM, Asylum Research, US) in the force volume (FV) mechanical imaging mode, mounting an AC160TS probe (Asylum Research) with 36N m^{-1} spring constant (obtained with built-in calibration). Average Young's modulus was obtained by measuring five different areas of the SA films. The mechanical properties of SA films were recorded by a universal tensile testing machine (HY-0580, Shanghai Hengyi Testing Instruments Co., Ltd., China). The physicochemical properties of the SA films were further characterized by the Fourier transform infrared spectroscopy (FTIR, Thermo Scientific Nicolet iS50, US), X-ray diffraction analysis (XRD, Rigaku Ultima IV, Japan), and 2D wide-angle X-ray diffraction (2D-WAXD, Xeuss 3.0, France).

Supporting Information

Supporting Information is available from the Wiley Online Library or from the author.

Acknowledgements

The authors acknowledge the financial support provided by the National Natural Science Foundation of China (52022102, 52261160380), National Key R&D Program of China (2017YFA0701303), the Youth Innovation Promotion Association of CAS (2019353), Guangdong Regional Joint Fund-Key Project (2021B1515120076), and the Fundamental Research Program of Shenzhen (RCJC20221008092729033, JCYJ20220818101800001).

Conflict of Interest

The authors declare no conflict of interest.

Author contributions

X.D. conceived the idea and designed the experiments. H.H. conducted the experiments with assistance from M.N.M.G. and X.Y. took AFM characterization. X.D. supervised the study, analyzed the results, and wrote the manuscript. All authors contributed to the discussion and interpretation of the results.

Data Availability Statement

The data that support the findings of this study are available in the supplementary material of this article.

Keywords

liquid metals, multi-responsive, recyclable materials, starch, soft actuators

Received: April 26, 2023
Revised: June 7, 2023
Published online:

[1] D. Rus, M. T. Tolley, *Nature* **2015**, *521*, 467.
[2] M. Li, A. Pal, A. Aghakhani, A. Pena-Francesch, M. Sitti, *Nat. Rev. Mater.* **2022**, *7*, 235.
[3] M. Cianchetti, C. Laschi, A. Menciassi, P. Dario, *Nat. Rev. Mater.* **2018**, *3*, 143.
[4] S. Palagi, P. Fischer, *Nat. Rev. Mater.* **2018**, *3*, 113.
[5] Q. L. Zhao, C. Li, H. C. Shum, X. M. Du, *Lab Chip* **2020**, *20*, 4321.
[6] Y. S. Zhang, A. Khademhosseini, *Science* **2017**, *356*, eaaf3627.
[7] F. F. Fu, L. R. Shang, Z. Y. Chen, Y. R. Yu, Y. J. Zhao, *Sci Robot* **2018**, *3*, eaar8580.
[8] X. M. Du, H. Q. Cui, B. Sun, J. Wang, Q. L. Zhao, K. Xia, T. Z. Wu, M. S. Humayun, *Adv. Mater. Technol.* **2017**, *2*, 1700120.
[9] H. C. Quan, D. Kisailus, M. A. Meyers, *Nat. Rev. Mater.* **2021**, *6*, 264.
[10] A. Lendlein, O. E. C. Gould, *Nat. Rev. Mater.* **2019**, *4*, 116.
[11] Y. L. Xia, Y. He, F. H. Zhang, Y. J. Liu, J. S. Leng, *Adv. Mater.* **2021**, *33*, 2000713.
[12] Q. L. Zhao, J. Wang, Y. L. Wang, H. Q. Cui, X. M. Du, *Natl Sci Rev* **2019**, *7*, 629.
[13] J. Wang, Q. L. Zhao, H. Q. Cui, Y. L. Wang, H. X. Chen, X. M. Du, *J. Mater. Chem. A* **2018**, *6*, 24748.
[14] A. H. Gelebart, D. J. Mulder, M. Varga, A. Konya, G. Vantomme, E. W. Meijer, R. L. B. Selinger, D. J. Broer, *Nature* **2017**, *546*, 632.
[15] K. Kumar, C. Knie, D. Bléger, M. A. Peletier, H. Friedrich, S. Hecht, D. J. Broer, M. G. Debije, A. P. H. J. Schenning, *Nat. Commun.* **2016**, *7*, 11975.
[16] J. A. Lv, Y. Y. Liu, J. Wei, E. Q. Chen, L. Qin, Y. L. Yu, *Nature* **2016**, *537*, 179.
[17] Y. L. Wang, Q. L. Zhao, X. M. Du, *Mater. Horiz.* **2020**, *7*, 1341.
[18] Z. W. Li, N. V. Myung, Y. D. Yin, *Sci Robot* **2021**, *6*, eabi4523.
[19] Y. S. Zhao, C. Y. Lo, L. C. Ruan, C. H. Pi, C. Kim, Y. Alsaid, I. Frenkel, R. Rico, T. C. Tsao, X. M. He, *Sci Robot* **2021**, *6*, eabd5483.
[20] S. Wang, Y. Gao, A. Wei, P. Xiao, Y. Liang, W. Lu, C. Y. Chen, C. Zhang, G. L. Yang, H. M. Yao, T. Chen, *Nat. Commun.* **2020**, *11*, 4359.
[21] X. L. Pang, J. A. Lv, C. Y. Zhu, L. Qin, Y. L. Yu, *Adv. Mater.* **2019**, *31*, 1904224.
[22] Y. L. Yu, T. Ikeda, *Angew. Chem., Int. Ed.* **2006**, *45*, 5416.
[23] Q. L. Zhao, J. Wang, H. Q. Cui, H. X. Chen, Y. L. Wang, X. M. Du, *Adv. Funct. Mater.* **2018**, *28*, 1801027.
[24] Z. L. Wu, M. Moshe, J. Greener, H. Therien-Aubin, Z. H. Nie, E. Sharon, E. Kumacheva, *Nat. Commun.* **2013**, *4*, 1586.
[25] L. D. Zhang, H. R. Liang, J. Jacob, P. Naumov, *Nat. Commun.* **2015**, *6*, 7429.
[26] J. Mu, J. Mu, G. Wang, H. P. Yan, H. Y. Li, X. M. Wang, E. Gao, C. Y. Hou, A. T. C. Pham, L. J. Wu, Q. H. Zhang, Y. G. Li, Z. P. Xu, Y. Guo, E. Reichmanis, H. Z. Wang, M. F. Zhu, *Nat. Commun.* **2018**, *9*, 590.
[27] Y. Dong, J. Wang, X. K. Guo, S. S. Yang, M. O. Ozen, P. Chen, X. Liu, W. Du, F. Xiao, U. Demirci, B. F. Liu, *Nat. Commun.* **2019**, *10*, 4087.
[28] M. M. Ma, L. Guo, D. G. Anderson, R. Langer, *Science* **2013**, *339*, 186.
[29] L. D. Zhang, P. Naumov, *Angew. Chem., Int. Ed.* **2015**, *54*, 8642.
[30] Y. L. Wang, H. Q. Cui, Q. L. Zhao, X. M. Du, *Matter* **2019**, *1*, 626.
[31] S. S. Wu, H. H. Shi, W. Lu, S. X. Wei, H. Shang, H. Liu, M. Q. Si, X. X. Le, G. Q. Yin, P. Theato, T. Chen, *Angew. Chem., Int. Ed.* **2021**, *60*, 21890.
[32] L. D. Zhang, P. e. Naumov, X. M. Du, Z. G. Hu, J. Wang, *Adv. Mater.* **2017**, *29*, 1702231.
[33] H. Na, Y. W. Kang, C. S. Park, S. Jung, H. Y. Kim, J. Y. Sun, *Science* **2022**, *376*, 301.
[34] X. M. Du, H. Q. Cui, T. T. Xu, C. Y. Huang, Y. L. Wang, Q. L. Zhao, Y. S. Xu, X. Y. Wu, *Adv. Funct. Mater.* **2020**, *30*, 1909202.
[35] J. C. Zhang, Y. B. Guo, W. Q. Hu, M. Sitti, *Adv. Mater.* **2021**, *33*, 2100336.
[36] F. Hartmann, M. Baumgartner, M. Kaltenbrunner, *Adv. Mater.* **2021**, *33*, 2004413.
[37] Q. Guo, E. Dai, X. Han, S. Xie, E. Chao, Z. Chen, *J R Soc Interface* **2015**, *12*, 20150598.
[38] L. C. T. Scorza, M. C. Dornelas, *Plant Signaling Behav.* **2011**, *6*, 1979.
[39] H. Q. Cui, Q. L. Zhao, L. Zhang, X. M. Du, *Adv Intell Syst* **2020**, *2*, 2000138.
[40] X. M. Du, H. Q. Cui, Q. L. Zhao, J. Wang, H. X. Chen, Y. L. Wang, *Research* **2019**, *2019*, 6398296.
[41] H. Hu, C. Huang, M. Galluzzi, Q. Ye, R. Xiao, X. F. Yu, X. M. Du, *Research* **2021**, *2021*, 9786128.
[42] S. S. Wang, Q. L. Zhao, J. H. Li, X. M. Du, *ACS Appl. Mater. Interfaces* **2022**, *14*, 42420.
[43] W. S. Ratnayake, D. S. Jackson, in *Advances in Food and Nutrition Research*, Academic Press, Pittsburgh, U.S.A **2008**.
[44] T. Cai, H. B. Sun, J. Qiao, L. L. Zhu, F. Zhang, J. Zhang, Z. J. Tang, X. L. Wei, J. G. Yang, Q. Q. Yuan, W. Y. Wang, X. Yang, H. Y. Chu, Q. Wang, C. You, H. W. Ma, Y. X. Sun, Y. Li, C. Li, H. F. Jiang, Q. H. Wang, Y. H. Ma, *Science* **2021**, *373*, 1523.
[45] H. C. Xiang, Z. J. Li, H. B. Liu, T. Chen, H. W. Zhou, W. Huang, *npj Flexible Electron.* **2022**, *6*, 15.
[46] M. Pooresmaeil, H. Namazi, *Carbohydr. Polym.* **2021**, *258*, 117654.
[47] H. Hu, F. J. Xu, *Biomater. Sci.* **2020**, *8*, 2084.
[48] S. Wan, N. Wu, Y. Z. Ye, S. B. Li, H. Z. Huang, L. Chen, H. C. Bi, L. T. Sun, *Small Struct.* **2021**, *2*, 2100105.
[49] J. B. Engel, A. Ambrosi, I. C. Tessaro, *Carbohydr. Polym.* **2019**, *225*, 115234.
[50] S. D. Zhang, Y. R. Zhang, X. L. Wang, Y. Z. Wang, *Starch – Stärke* **2009**, *61*, 646.
[51] E. Ojogbo, E. O. Ogunsona, T. H. Mekonnen, *Mater. Today Sustainability.* **2020**, *7–8*, 100028.
[52] L. Wang, X. H. Zhang, K. Yang, Y. V. Fu, T. S. Xu, S. L. Li, D. W. Zhang, L. N. Wang, C. S. Lee, *Adv. Funct. Mater.* **2020**, *30*, 1904156.
[53] F. Wang, M. J. Liu, C. Liu, Q. L. Zhao, T. Wang, Z. K. Wang, X. M. Du, *Sci. Adv.* **2022**, *8*, eabp9369.
[54] F. Wang, M. J. Liu, C. Liu, C. Huang, L. D. Zhang, A. Y. Cui, Z. G. Hu, X. M. Du, *Natl. Sci. Rev.* **2023**, *10*, nwac164.
[55] J. E. Park, H. S. Kang, M. Koo, C. Park, *Adv. Mater.* **2020**, *32*, 2002178.
[56] P. L. Li, A. Kierulf, J. Y. Wang, M. Yaghoobi, J. Whaley, J. Smoot, M. P. Herrera, A. Abbaspourrad, *ACS Appl. Mater. Interfaces* **2022**, *14*, 24955.
[57] Q. F. Zhong, B. B. Gao, Y. X. Weng, S. D. Zhang, *ACS Sustainable Chem. Eng.* **2022**, *10*, 3661.
[58] B. Wang, W. Gao, X. M. Kang, Y. P. Dong, P. F. Liu, S. X. Yan, B. Yu, L. Guo, B. Cui, A. M. Abd El-Aty, *Food Hydrocolloids* **2021**, *118*, 106760.
[59] W. Wang, L. Yao, T. Zhang, C.-Y. Cheng, D. Levine, H. Ishii, Proceedings of the 2017 CHI conference on human factors in computing systems **2017**, 6123.
[60] D. Dutta, N. Sit, *Starch – Stärke* **2022**, *74*, 2200110.
[61] X. K. Li, M. J. Li, J. Xu, J. You, Z. Q. Yang, C. X. Li, *Nat. Commun.* **2019**, *10*, 3514.

